Molybdenum Disulfide/Nitrogen-Doped Reduced Graphene Oxide Nanocomposite with Enlarged Interlayer Spacing for Electrocatalytic Hydrogen Evolution

Yu-Jia Tang, Yu Wang, Xiao-Li Wang, Shun-Li Li, Wei Huang, Long-Zhang Dong, Chun-Hui Liu, Ya-Fei Li,* and Ya-Qian Lan*

Facile design of low-cost and highly active catalysts from earth-abundant elements is favorable for the industrial application of water splitting. Here, a simple strategy to synthesize an ultrathin molybdenum disulfide/nitrogen-doped reduced graphene oxide (MoS_2/N-RGO-180) nanocomposite with the enlarged interlayer spacing of 9.5 Å by a one-step hydrothermal method is reported. The synergistic effects between the layered MoS_2 nanosheets and N-doped RGO films contribute to the high activity for hydrogen evolution reaction (HER). MoS_2/N-RGO-180 exhibits the excellent catalytic activity with a low onset potential of −5 mV versus reversible hydrogen elelctrode (RHE), a small Tafel slope of 41.3 mV dec^{-1}, a high exchange current density of 7.4×10^{-4} A cm^{-2}, and good stability over 5 000 cycles under acidic conditions. The HER performance of MoS_2/N-RGO-180 nanocomposite is superior to the most reported MoS_2-based catalysts, especially its onset potential and exchange current density. In this work, a novel and simple method to the preparation of low-cost MoS_2-based electrocatalysts with the extraordinary HER performance is presented.

1. Introduction

Hydrogen (H_2), as the clean and promising alternatives to fossil fuels, has drawn extensive attention because of the growing global energy and environmental crisis.[1,2] The cathodic reaction of electrochemical water splitting–hydrogen evolution reaction (HER) offers an effective process to produce H_2 from water in bulk.[3] Although most effective electrocatalysts for HER are Pt-based materials, the high-cost and limited crustal abundance of noble metals have hindered their industrial mass production.[4–6] Thus, it is urgent to develop active, inexpensive, and earth-abundant HER electrocatalysts for realizing the blueprint of "hydrogen economy."

In recent years, remarkable works have been focused on the exploration of non-noble metal electrocatalysts for HER, such as chalcogenides,[7–9] phosphides,[10,11] carbides,[12] nitrides,[13,14] alloys,[15,16] and metal-free catalysts.[17,18] Transition metal dichalcogenides (TMDs) present remarkable performances as the HER electrocatalysts because of the low-cost and edge-terminated structure among 2D materials.[9,19,20] TMDs are a class of materials with the formula MX_2, where M is the transition metal (Mo or W) and X is the chalcogen (S or Se).[21] As a typical layered TMD material, molybdenum disulfide (MoS_2) has gained great attention and been extensively used as the HER catalyst recently, which shows several S-Mo-S layers through weak van der Waals interactions.[22,23] Both theoretical and experimental researches have demonstrated that MoS_2 has the catalytic active sites serving as the HER electrocatalyst.[24,25] Although the HER performance of MoS_2-based materials has been reported in quantity, the HER activity still cannot be compared with Pt-based catalysts, especially the onset potential, because of the severe stacking of MoS_2 layers and its poor stability. Recently, researchers have found that regulating the interlayer spacing of MoS_2 can change the HER performance of these MoS_2-based catalysts. Xie et al.[26] reported the oxygen-incorporated MoS_2 ultrathin nanosheets with the large interlayer spacing of 9.5 Å, which show a moderate degree of disorder and the Tafel slopes of 50–55 mV dec^{-1}. Besides, Sun and co-workers[27] synthesized MoS_2 nanosheets with the expanded interlayer spacing of 9.4 Å and edge-terminated structure using a mircowave-assisted strategy, possessing a good HER activity with the onset potential of −103 mV. Thus, increasing the interlayer spacing of MoS_2 by introducing the small molecules or changing the reaction conditions can truly improve the HER activity.

Graphene, a single layer of graphite, has been reported to be an ideal HER electrocatalyst when coupled with other metal-based materials because of its high electric/thermal conductivity and large specific surface area.[28,29] Besides, the HER activity of MoS_2 is limited by its poor electrical conductivity and low electron transfer capability which

Y.-J. Tang, Y. Wang, X.-L. Wang, Prof. S.-L. Li,
W. Huang, L.-Z. Dong, C.-H. Liu, Prof. Y.-F. Li,
Prof. Y.-Q. Lan
Jiangsu Key Laboratory of Biofunctional Materials
College of Chemistry and Materials Science
Nanjing Normal University
Nanjing 210023, P. R. China
E-mail: liyafei.abc@gmail.com; yqlan@njnu.edu.cn

intrinsically originated from the large bandgap.[21] Thus, introducing the conductive graphene substrates into MoS_2-based materials could increase the surface area and accelerate the electron transfer.[30,31] To date, MoS_2/graphene composites have been widely reported as the electrode materials of Li-ion batteries,[32] photocatalysis,[33] and so on. Moreover, researches have shown that doping graphene materials with heteroatoms (e.g., N, P) have great effects on the HER performance because of the electronic structure change.[34] Therefore, if we can control the interlayer spacing of MoS_2 while synthesizing MoS_2/heteroatom-doped graphene nanocomposite, the high-efficient HER electrocatalysts are expected to be obtained. In contrast with pure MoS_2, the interlayer spacing in MoS_2/heteroatom-doped graphene nanocomposite is harder to control because of the complication and diversity of the MoS_2-based nanocomposite systems. Thus, it is a great challenge to synthesize uniformly MoS_2/heteroatom-doped graphene nanocomposite with enlarged interlayer spacing.

In this work, we have synthesized molybdenum disulfide/nitrogen-doped reduced graphene oxide (MoS_2/N-RGO-180) nanocomposite with enlarged interlayer spacing of 9.5 Å by controlling the hydrothermal temperature easily using phosphomolybdic acid (PMo_{12}), graphene oxide (GO), and thiourea as precursors. The polyoxometalates (POMs) are the kinds of cations and polyanion clusters with the polynuclear metal-oxo structure.[35,36] Among them, PMo_{12} is an anionic Keggin-type POM with the diameter less than 1 nm, which has good water-solubility and strong reversible oxidization properties. Therefore, PMo_{12} particles can disperse in the interlayers of GO solutions homogenously because of the electrostatic repulsion.[37] After adding thiourea into the PMo_{12}/GO solutions, MoS_2 nanosheets with expanded interlayer spacing could be formed in situ uniformly during the hydrothermal reaction because GO films are used as the nucleation sites. At the same time, GO could be reduced to RGO because of the strong reducibility of PMo_{12}. Excessive thiourea precursors could be decomposed to NO_2 gases to react with GO films, forming N-doped RGO films and rich-defect structure.[38] The nitrogen doped species (0.906 wt%) would enhance the HER activity dramatically because heteroatoms doping can modulate electrons to improve the chemical activities.[39,40] It is the first time to synthesize MoS_2-based nanocomposite at different hydrothermal temperatures using PMo_{12}, thiourea, and GO as precursors, which shows different interlayer spacing of MoS_2 nanosheets from 6.2 to 9.5 Å. Surprisingly, MoS_2/N-RGO-180 nanocomposite with enlarged interlayer spacing of 9.5 Å exhibits the most positive onset potential among all reported MoS_2-based materials prepared with hydrothermal method when using as HER electrocatalyst in acidic electrolyte. MoS_2/N-RGO-180 composite shows a small onset potential of ≈−5 mV versus RHE, a low Tafel slope of 41.3 mV dec^{-1}, a high exchange current density of 7.4 × 10^{-4} A cm^{-2}. and long-term stability in acidic electrolyte.

2. Results and Discussion

Herein, all samples are named as MoS_2/N-RGO-T or MoS_2-T, where T means the reaction temperature in °C. And RGO loadings are always 10 wt% if not specified. As illustrated in **Figure 1**, PMo_{12} particles are dispersed homogenously in GO solution by ultrasonication for several minutes. Then thiourea precursors are added to the above solution and the mixtures are transferred to a Teflon-lined autoclave reacting by the hydrothermal method. MoS_2/N-RGO nanocomposite obtained at 160 or 180 °C for 24 h has the enlarged interlayer spacing of 9.5 Å. However, when increasing the reaction temperature higher than 180 °C, the interlayer spacing of MoS_2 nanosheet for MoS_2/N-RGO nanocomposite would decrease to 6.2 Å. In addition, we also have synthesized MoS_2/N-RGO samples with different molar ratios, concentration ratios, GO loadings, and reaction temperatures. Individual MoS_2-T samples without GO have also been synthesized (experimental section in the Supporting Information).

The powder X-ray diffraction (XRD) patterns of MoS_2/N-RGO-T nanocomposites synthesized at different temperatures (160–220 °C) are shown in **Figure 2**a. As can be seen, MoS_2/N-RGO-200 and MoS_2/N-RGO-220 that prepared at higher temperature match very well with the standard pattern of 2H-MoS_2 (Joint Committee on Powder Diffraction Standards, JCPDS card no. 75–1539). The broad peak centered at 14.2° is the (002) diffraction peak with the interlayer spacing of 6.2 Å. However, when the reaction temperature is relatively low (160 and 180 °C), two new diffraction peaks can be observed at 9.3° and 18.6°, which show the interlayer spacing of 9.5 and 4.7 Å, respectively, according to the computational simulations.[26] Besides, MoS_2-T materials prepared without GO films also have the same phenomenon (Figure S2a, Supporting Information). Figure 2b shows the transmission electron microscope (TEM) image of MoS_2/N-RGO-180 nanocomposite, which confirms MoS_2 nanosheets have an intimate contact on RGO films without agglomeration. As can be seen, MoS_2 thin nanosheets with the diameter of ≈100 nm are distributed on the surface of RGO films homogenously, while MoS_2/N-RGO-T composites obtained at higher temperatures are likely to aggregate into thick materials (Figure S3, Supporting Information). The selected-area electron diffraction (SAED) pattern (Figure 2b inset) reveals the polycrystallinity of MoS_2/N-RGO-180 nanocomposite with concentric rings. The high resolution TEM (HRTEM) image of MoS_2/N-RGO-180 (Figure 2c) shows the
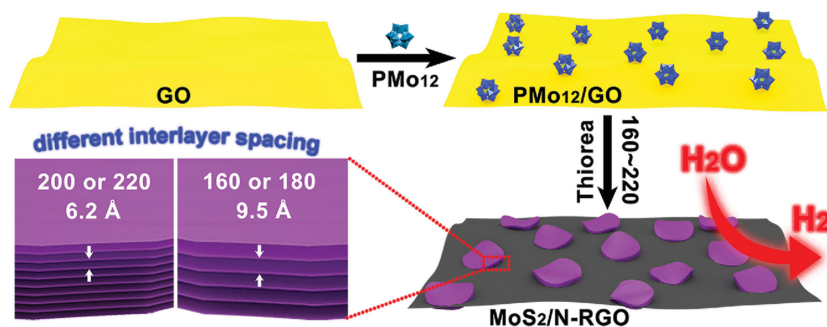

Figure 1. Schematic preparation process of MoS_2/N-RGO-T nanocomposite.
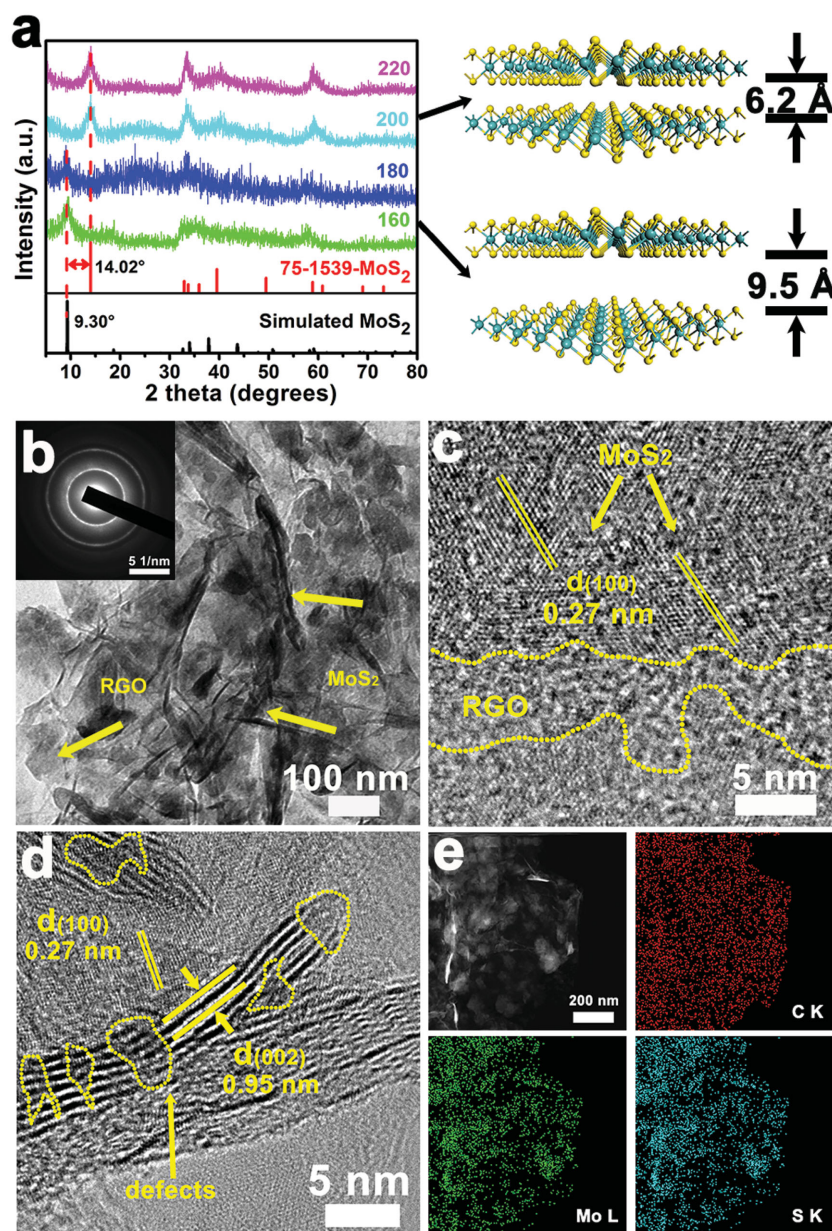
Figure 2. a) XRD patterns of MoS$_2$/N-RGO-T nanocomposite prepared at different temperatures from 160 to 220 °C. At the right, structural models of MoS$_2$ with the interlayer spacing of 6.2 and 9.5 Å, respectively. b) TEM image of MoS$_2$/N-RGO-180. The inset is the corresponding SAED pattern. c,d) HRTEM of MoS$_2$/N-RGO-180. e) Element mapping images of MoS$_2$/N-RGO-180, indicating the homogeneous distribution of C, Mo, and S.

the total number of active sites obviously. When reacting with high pressure and temperature (≤180 °C) in the autoclave, excessive thiourea can be decomposed into NH$_3$ molecules which can intercalate into MoS$_2$ ultrathin nanosheets uniformly. Besides, the hydrothermal solvent is acidic because of the existence of PMo$_{12}$, which makes NH$_3$ molecules into NH$_4^+$ ions. According to the Scherrer equation, the interlayer spacing of MoS$_2$/N-RGO nanocomposite synthesized at temperature of 160 or 180 °C has increased 3.3 Å comparing with the pristine 2H-MoS$_2$, which matches well with the size of NH$_4^+$ ions whose diameter is about 3.5 Å. Therefore, NH$_4^+$-incorporated MoS$_2$/N-RGO nanocomposites show the enlarged interlayer spacing of 9.5 Å. However, when increasing the hydrothermal temperature up to 200 °C, the interlayer spacing is reduced to 6.2 Å because the inserted NH$_4^+$ ions would be released from the layers of MoS$_2$ at higher temperature (200 and 220 °C). Elemental mappings of MoS$_2$/N-RGO-180 (Figure 2e) indicate the uniformly distribution of C, Mo, and S elements. HRTEM images and element mapping of MoS$_2$-180 without RGO films are also shown in Figure S4 (Supporting Information). Besides, all MoS$_2$/ N-RGO-T and MoS$_2$-T samples have been characterized by energy dispersive X-ray, which show the existence of C, O, Mo, S, as well as a little P elements (Figures S5 and S6, Supporting Information).

Upon employing scanning electron microscopy (SEM) to observe the morphology, it can be seen that MoS$_2$/N-RGO-160 and MoS$_2$/ N-RGO-180 nanocomposites are ultrathin wrinkles including MoS$_2$ nanosheets and RGO films to form the 3D porous structures. According to SEM images shown in the inset of Figure S7a,b (Supporting Information), the thickness of these two samples are only several nanometers. However, when increasing the reaction temperatures to 200 or 220 °C, MoS$_2$/N-RGO-T begin to agglomerate and stack into thick materials (Figure S7c,d, Supporting Information), which leading to the decreasing of the surface areas and the numbers of active sites. In contrast, TEM and SEM images (Figures S8 and S9, Supporting Information) of MoS$_2$-T materials prepared at different temperatures all tend to stack into the flower-like agglomerations because of the interlayer van der Waals attraction and the high surface energy between MoS$_2$ films without RGO substrates.[8] In addition, the Brunauer–Emmett–Teller specific surface areas of MoS$_2$-180 and MoS$_2$/N-RGO-180 obtained from N$_2$ adsorption isotherms are 39.0 and 117.9 m^2 g^{-1}, respectively, suggesting that RGO films can increase the surface area obviously (Figure S10, Supporting Information). The pore diameter

distinct limitations of amorphous RGO films and the lattice space (d) of 0.27 nm assigning to the (100) plane of MoS$_2$. Furthermore, Figure 2d demonstrates only a few layers (≈7 layers) stacked MoS$_2$ nanosheets with the enlarged interlayer spacing of 9.5 Å and rich defects for MoS$_2$/N-RGO-180, which is consistent with the above XRD results. Because the numbers of MoS$_2$ layers are similar and uncertain (5–9 layers) for different MoS$_2$/N-RGO-T samples, the main factor to affect HER activities is not the numbers of layers but the interlayer spacing. Conventional interlayer spacing (6.2 Å) expose less active sites while the enlarged interlayer spacing (9.5 Å) make the increasing of

distributions calculated by Barrett–Joyner–Halenda method indicate the presence of mesopores around 4 nm of these two materials.

Raman spectrum of MoS_2/N-RGO-180 nanocomposite (Figure S11a, Supporting Information) shows the D-band (1363 cm^{-1}) and G-band (1592 cm^{-1}) for RGO films. The value of I_D/I_G peak intensity is 0.86, indicating that the hydrothermal reaction conditions have increased the crystallinity of RGO films. The enlarged Raman spectrum of MoS_2/N-RGO-180 and MoS_2-180 (Figure S11b, Supporting Information) presents the in-plane E^1_{2g} and the out-of-plane A_{1g} peaks at 383 and 411 cm^{-1}, respectively, which are the characteristic peaks of the pristine 2H-MoS_2.[41,42] Besides, the intensity of A_{1g} mode is higher than the E^1_{2g} mode, indicating that MoS_2/N-RGO-180 have abundant edge-terminated structures and decreased number of S-Mo-S layers.[27]

X-ray photoelectron spectroscopy (XPS) spectrum can be used to analyze the surface chemistry of MoS_2/N-RGO-180 nanocomposite. **Figure 3**a shows the XPS spectrum of MoS_2/N-RGO-180 nanocomposite with existence of C, Mo, S, N, and O elements. The C1s XPS spectrum of MoS_2/N-RGO-180 nanocomposite (Figure 3b) has a strong peak of C—C/C=C species (284.6 eV) and two relatively weak peaks of C—N (285.2 eV) and C—O (286.4 eV), which demonstrate the heteroatom doping and the reduction of GO to RGO films. Mo3d spectrum (Figure 3c) presents a weak peak of S2s (225.9 eV) and two characteristic peaks of $Mo3d_{3/2}$ (232.0 eV) and $Mo3d_{5/2}$ (228.9 eV), indicating the Mo (IV) oxidation state for MoS_2. Besides, the other two relatively weak peaks at 235.9 eV and 233.2 eV are $Mo3d_{3/2}$ and $Mo3d_{5/2}$ binding energies for the Mo (VI) oxidation state, respectively. The S2p XPS spectrum (Figure 3d) shows two main peaks at 162.8 and 161.6 eV, which are attribute to the $S2p_{1/2}$ and $S2p_{3/2}$ binding energies for S^{2-}, respectively. And the peak at 169.0 eV is the small amount of SO_4^{2-} residues. The high-resolution N1s spectrum (Figure 3e) reveals the existence of the pyridinic N (398.2 eV), graphic N (401.7 eV), and Mo3p peak (394.7 eV). According to the peak area, pyridinic N may be the main nitrogen species of MoS_2/N-RGO-180 nanocomposite, because it has a lone electron pair in the plane of carbon matrix and can donate the electrons to adsorb hydrogen. As shown in Figure 3f, the peaks for O1s spectrum are observed at 533.3, 532.2, 531.4, and 530.7 eV assigning to C—OH, Mo—O, C—O/O—C—N and O=C bonds, respectively. We also show the XPS spectra of MoS_2-180 in Figure S12 (Supporting Information). According to the XPS analysis, the mass percent of element C and S are 20.6 wt% and 17.6 wt%, respectively, while the mass percent of MoS_2 is 43.9 wt% for MoS_2/N-RGO-180 (Table S3, Supporting

Information). Moreover, the N content is measured to be 0.906 wt% by elemental analyzer (Table S2, Supporting Information) because XPS analysis cannot distinguish the content Mo and N precisely. Therefore, the N-doped species account for 4.4 wt% of carbon contents suggesting the rich N doping in MoS_2/N-RGO-180 nanocomposite.

The HER performance was investigated in 0.5 M H_2SO_4 solution (N_2 saturated) with a typical three-electrode system. The catalysts were loaded directly on glassy carbon electrode with the amount of 0.14 mg cm^{-2} and all the linear sweep voltammetry were obtained at the scan rate of 5 mV s^{-1}. At first, the HER activity of MoS_2/N-RGO-180 with different GO loadings are studied and 10 wt% GO loadings show the best HER activity (Figure S13, Supporting Information). In comparison, we have tested the commercial 20% Pt/C and MoS_2/N-RGO-T catalysts synthesized at different temperatures (160–220 °C) (**Figure 4**a). When the reaction temperature is less than or equal to 180 °C, the polarization curves show relatively low onset potentials and tremendously enhanced current densities. However, the HER activities become poor when increasing the reaction temperature higher than or equal to 200 °C. Surprisingly,
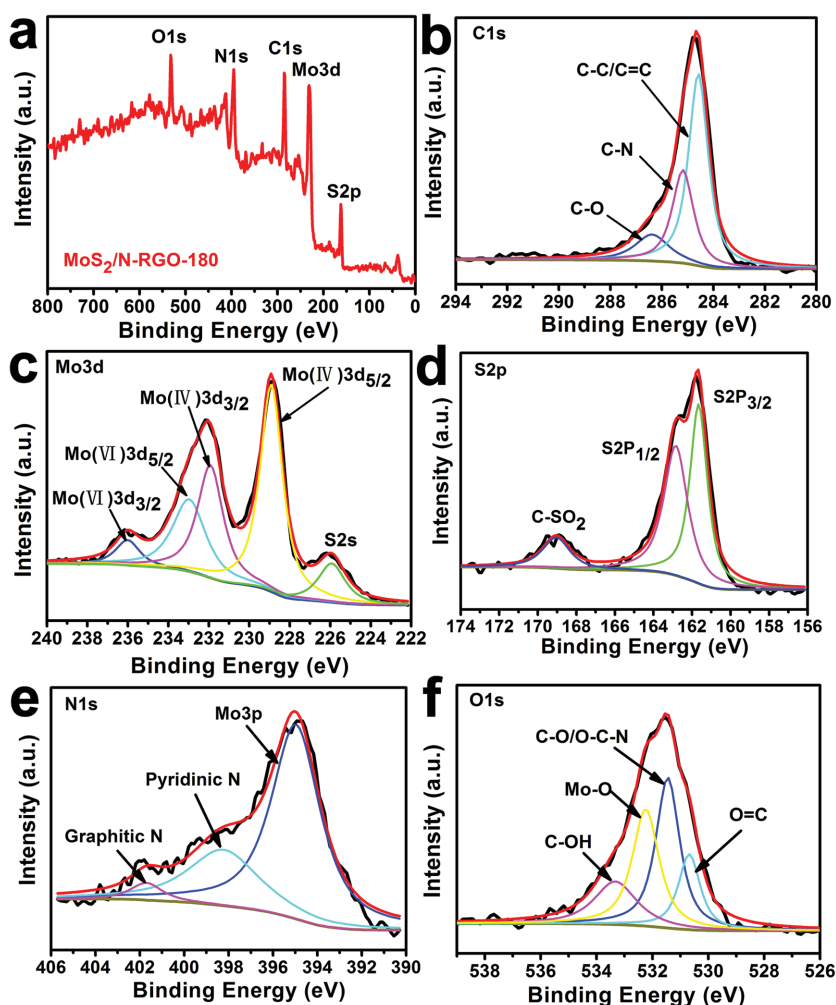

Figure 3. XPS spectrum of a) MoS_2/N-RGO-180 nanocomposite. High-resolution XPS spectra of b) C1s, c) Mo3d, d) S2p, e) N1s, and f) O1s of MoS_2/N-RGO-180.
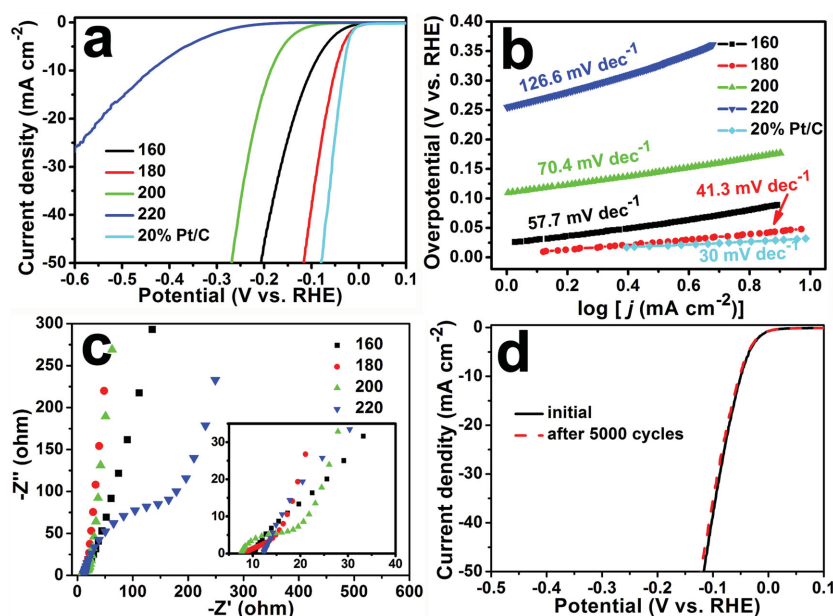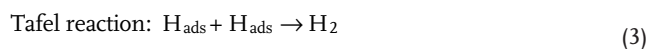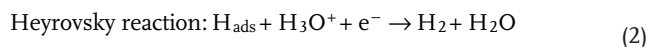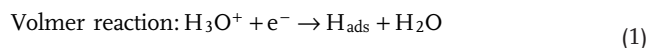
Figure 4. a) Polarization curves and b) corresponding Tafel plots of MoS$_2$/N-RGO-T prepared at different temperatures and commercial 20% Pt/C catalyst. Catalyst loading is 0.14 mg cm^{-2}. Electrolyte is N$_2$-saturated 0.5 M H$_2$SO$_4$. Scan rate is 5 mV s^{-1}. c) Nyquist plots of different samples over the frequency range from 1000 kHz to 10 mHz at the open-circuit voltage with an AC voltage of 10 mV. The inset shows the enlarged nyquist plots. d) Cycling stability of MoS$_2$/N-RGO-180 before and after 5 000 CV cycles from −50 to −250 mV versus RHE at the scan rate of 100 mV s^{-1}.

MoS$_2$/N-RGO-180 nanocomposite has the onset potential of only −5 mV versus RHE, outperforming all MoS$_2$-based HER catalysts that are prepared using the hydrothermal methods, such as MoS$_2$/CoSe$_2$,[7] oxygen-incorporated MoS$_2$ ultrathin nanosheets,[26] MoS$_2$/RGO hybrid,[30] MoS$_2$/RGO$_2$,[31] and MoS$_2$ nanosheets vertically grow on carbon cloth (MoS$_2\perp$CC).[43] In addition, the overpotential at the current density of 10 mA cm^{-2} (η_{10}) is also an important parameter for the comparison of the HER activities with various electrocatalysts. MoS$_2$/N-RGO-180 catalyst only requires the overpotential of 56 mV to reach the value of 10 mA cm^{-2}, while η_{10} of MoS$_2$/N-RGO-160, MoS$_2$/N-RGO-200, and MoS$_2$/N-RGO-220 are 107, 192, and 445 mV, respectively (**Table 1**). Furthermore, the electrocatalytic activity of MoS$_2$/N-RGO-180 is also superior to the most reported MoS$_2$-based catalysts, especially the values of onset potential and η_{10} (Table S4, Supporting Information). Besides, MoS$_2$-T catalysts without RGO films have been tested and shown relatively poor HER activities (Figure S14, Supporting Information). Highly conductive N-RGO-180 catalyst without adding Mo

sources also has been compared with MoS$_2$/N-RGO-180 and exhibits a negative onset potential of −192 mV versus RHE and a large Tafel plot of 79.2 mV dec^{-1} (Figure S15, Supporting Information). In order to see the hydrogen evolution clearly, we have coated MoS$_2$/N-RGO-180 catalyst on the stainless steel mesh which is used as the current collector. Along with the increasing applied voltage, it would release H$_2$ gas bubbles quickly from the surface of the electrocatalyst (Figure S16 and Video S1, Supporting Information).

Tafel slope is an inherent parameter to evaluate the HER performance, which can be calculated using the Tafel equation ($\eta = b \log j + a$, where η is the overpotential, b is the Tafel slope, j is the current density and a is the constant). The Tafel slopes of MoS$_2$/N-RGO-T prepared from 160 to 220 °C are 57.7, 41.3, 70.4, and 126.6 mV dec^{-1}, respectively (Figure 4b). According to the mechanism of hydrogen evolution, there are three principal steps for HER in acidic electrolytes, including the Volmer, the Heyrovsky, and the Tafel steps, which can elucidate the electron transfer kinetics.[44,45] Three possible reactions are given in Equations (1)–(3)

$$\text{Volmer reaction: } H_3O^+ + e^- \rightarrow H_{ads} + H_2O \tag{1}$$

$$\text{Heyrovsky reaction: } H_{ads} + H_3O^+ + e^- \rightarrow H_2 + H_2O \tag{2}$$

$$\text{Tafel reaction: } H_{ads} + H_{ads} \rightarrow H_2 \tag{3}$$

Volmer reaction (Equation (1)) is known as the initial discharge step and its Tafel slope is 120 mV dec^{-1}. After that, it happens Heyrovsky reaction (Equation (2), the electrochemical desorption step) or Tafel reaction (Equation (3), the recombination step), which give the Tafel slope of 40 and 30 mV dec^{-1}, respectively.[46] Accordingly, the observed Tafel slope value of MoS$_2$/N-RGO-180 catalyst is the smallest except for the commercial 20% Pt/C catalyst (30 mV dec^{-1}), suggesting that the Volmer–Heyrovsky reaction mechanism dominates in the HER process and the electrochemical desorption is the rate determining step. Polarization curves and Tafel slopes of MoS$_2$/N-RGO-180 nanocomposites prepared with different molar ratios

Table 1. Electrochemical parameters of MoS$_2$/N-RGO-T nanocomposites prepared at different temperatures and commercial 20% Pt/C catalyst.

	Onset potential [mV]	η_{10} [mV]	Tafel slope [mV dec^{-1}]	j_0 [A cm^{-2}]	R_{ct} [ohm]
20% Pt/C	0	38	30	1.1×10^{-3}	–
MoS$_2$/N-RGO-180	−5	56	41.3	7.2×10^{-4}	10.6
MoS$_2$/N-RGO-160	−22	107	57.7	3.9×10^{-4}	13.4
MoS$_2$/N-RGO-200	−100	192	70.4	3.2×10^{-5}	17.6
MoS$_2$/N-RGO-220	−205	445	126.6	1.6×10^{-5}	181.5

and concentration ratios have also been compared in Figure S17 (Supporting Information).

Exchange current density (j_0) can be obtained by the extrapolation method on the basis of the Tafel equation (Figure S18, Supporting Information).[47] The j_0 value of MoS$_2$/RGO-180 catalyst is calculated to be 7.2×10^{-4} A cm^{-2}, which is higher than those of MoS$_2$/N-RGO-160 (3.9×10^{-4} A cm^{-2}), MoS$_2$/N-RGO-200 (3.2×10^{-5} A cm^{-2}), MoS$_2$/N-RGO-220 (1.6×10^{-5} A cm^{-2}), and slightly lower than the commercial 20% Pt/C (1.1×10^{-3} A cm^{-2}) (Table 1). Besides, we also estimate the electrochemical surface area of MoS$_2$/N-RGO-180 and MoS$_2$-180 by calculating the electrochemical double-layer capacitance (C_{dll}) (Figure S19, Supporting Information). The C_{dll} value of MoS$_2$/N-RGO-180 is 13.2 mF cm^{-2}, which is higher than MoS$_2$-180 (0.26 mF cm^{-2}), suggesting that MoS$_2$/N-RGO-180 nanocomposite has more active surface area and better HER performance.

Electrochemical impedance spectroscopy (Figure 4c) was used to reveal the HER kinetics at the electrode/electrolyte interface of the electrocatalysts. The R_{ct} values of different MoS$_2$/N-RGO-T samples listed in Table 1 indicate that enhanced HER performance is related to the lower charge-transfer resistance. Because of the highly conductive surface and strong hydrogen adsorption capacity, MoS$_2$/N-RGO-180 catalyst only has the R_{ct} of 10.6 Ω, which revealing the fast electron transfer rate between the interfaces and exhibiting an excellent HER activity in acidic electrolyte. In sharp contrast, MoS$_2$-T prepared without RGO films present very large R_{ct} values (Figure S14c,d, Supporting Information), which have low conductivities and poor HER performance. Stability is also a crucial parameter to determine the durable operation of HER electrocatalysts. The long-term stability of MoS$_2$/N-RGO-180 was tested using the cyclic voltammetry (CV) technique from −50 to −250 mV versus RHE scanning for 5 000 cycles at the scan rate of 100 mV s^{-1}. There is almost no active loss to be observed for the related polarization curves before and after 5 000 CV cycles in Figure 4d, indicating that MoS$_2$/N-RGO-180 is ultrastable in acidic electrolyte.

Density functional theory (DFT) calculations were further performed to better understand the different HER reactivity in MoS$_2$ with different interlayer spacing. In principle, the HER pathway can be depicted as a three-state diagram, which includes an initial state (H$^+$ + e$^-$), an intermediate state (adsorbed H, H*), and product (1/2 H$_2$).[18,48,49] Theoretically, the free energy change for hydrogen adsorption (ΔG_{H*}) is a good indicator for HER catalyst and the optimum value of ΔG_{H*} should be zero. **Figure 5** shows the calculated free energy diagram for hydrogen adsorption on two MoS$_2$ nanosheets with different interlayer spacing. Obviously, compared with the ordinary MoS$_2$ nanosheet with an interlayer spacing of 6.2 Å (−0.201 eV), the MoS$_2$ nanosheet with an enlarged interlayer spacing of 9.5 Å can present a more preferable ΔG_{H*} value of −0.052 eV, which can provide a fast proton/electron adsorption as well as a fast hydrogen release process. Therefore, due to the advantage of ultrafast kinetics, MoS$_2$ nanosheet with enlarged interlayer spacing of 9.5 Å shows more superior HER activity than the ordinary MoS$_2$ nanosheet. The theoretical results agree well with the above experimental measurements and further prove that the enlarged interlayer spacing can significantly improve the HER activity.
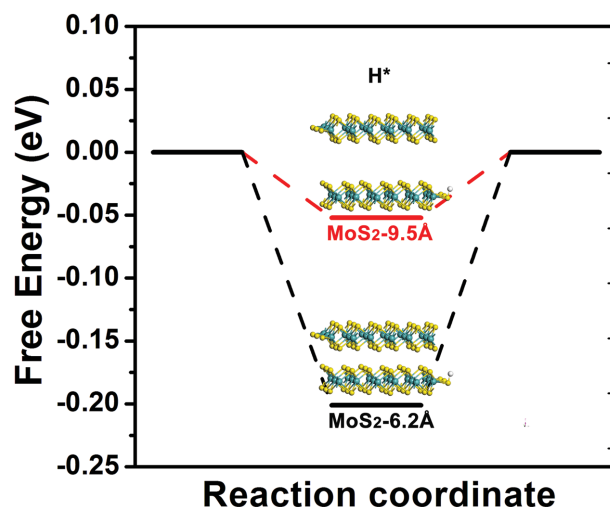

Figure 5. Calculated free energy diagram for HER on MoS$_2$-6.2 Å and MoS$_2$-9.5 Å.

Further studies on the HER kinetics indicate that such highly active HER performance can be ascribed to the synergistic effects among the enlarged lamellar structure of defect-rich MoS$_2$ nanosheets, highly conductive RGO substrates and pyridinic N species. First, MoS$_2$ thin films with rich defects and large interlayer spacing of 9.5 Å are the main active species for the HER. Because of this remarkable structure, MoS$_2$ could offer large amounts of active sites and provide more channels to speed the electron transfer for the HER. Second, RGO films could form the mesoporous networks with high conductivity and large surface area, thus facilitating the rapid diffusion of electrolyte into the interlayers of MoS$_2$/N-RGO-180 nanocomposite. Third, N-doped within carbon frameworks of RGO films, especially the pyridinic N species, can change the electronic structure to form the active centers, also improve the HER activity as well. In general, MoS$_2$/N-RGO-180 nanocomposite with ultrathin conductive networks and rich active sites is favorable for the electrocatalytic hydrogen evolution.

3. Conclusion

In summary, we have successfully synthesized MoS$_2$/N-RGO nanocomposites with different interlayer spacing using a facile hydrothermal method by changing the reaction temperature. Because of the unique ultrathin nanostructures with the enlarged interlayer spacing of 9.5 Å, MoS$_2$/N-RGO-180 electrocatalyst ensures the fast electron transfer and high-efficient H$_2$ production for HER. It is one of the best HER electrocatalysts among all the MoS$_2$-based materials, especially its onset potential and j_0, which exhibiting a very low onset potential of 5 mV versus RHE, a small Tafel slope of 41.3 mV dec^{-1}, a high exchange current density of 7.4×10^{-4} A cm^{-2}, and long-term stability. DFT calculations also have proved that MoS$_2$-9.5 Å with larger interlayer spacing show higher HER activity than MoS$_2$-6.2 Å. This method opens up a simple pathway to prepare 2D non-noble metal nanostructures using POMs as well as is favorable to the synthesis of other low-cost and highly active catalysts abundantly.

Supporting Information

Acknowledgements

[1] M. S. Dresselhaus, I. L. Thomas, *Nature* **2001**, *414*, 332.

[2] J. A. Turner, *Science* **2004**, *305*, 972.

[3] M. G. Walter, E. L. Warren, J. R. McKone, S. W. Boettcher, Q. Mi, E. A. Santori, N. S. Lewis, *Chem. Rev.* **2010**, *110*, 6446.

[4] N. P. Dasgupta, C. Liu, S. Andrews, F. B. Prinz, P. Yang, *J. Am. Chem. Soc.* **2013**, *135*, 12932.

[5] E. Antolini, *Energy Environ. Sci.* **2009**, *2*, 915.

[6] X. Zou, Y. Zhang, *Chem. Soc. Rev.* **2015**, *44*, 5148.

[7] M.-R. Gao, J.-X. Liang, Y.-R. Zheng, Y.-F. Xu, J. Jiang, Q. Gao, J. Li, S.-H. Yu, *Nat. Commun.* **2015**, *6*, 5982.

[8] J. Kibsgaard, Z. Chen, B. N. Reinecke, T. F. Jaramillo, *Nat. Mater.* **2012**, *11*, 963.

[9] C. G. Morales-Guio, X. Hu, *Acc. Chem. Res.* **2014**, *47*, 2671.

[10] Z. Xing, Q. Liu, A. M. Asiri, X. Sun, *Adv. Mater.* **2014**, *26*, 5702.

[11] E. J. Popczun, J. R. McKone, C. G. Read, A. J. Biacchi, A. M. Wiltrout, N. S. Lewis, R. E. Schaak, *J. Am. Chem. Soc.* **2013**, *135*, 9267.

[12] P. Xiao, X. Ge, H. Wang, Z. Liu, A. Fisher, X. Wang, *Adv. Funct. Mater.* **2015**, *25*, 1520.

[13] B. Cao, G. M. Veith, J. C. Neuefeind, R. R. Adzic, P. G. Khalifah, *J. Am. Chem. Soc.* **2013**, *135*, 19186.

[14] H. Yan, C. Tian, L. Wang, A. Wu, M. Meng, L. Zhao, H. Fu, *Angew. Chem. Int. Ed.* **2015**, *127*, 6423.

[15] J. Greeley, T. F. Jaramillo, J. Bonde, I. Chorkendorff, J. K. Norskov, *Nat. Mater.* **2006**, *5*, 909.

[16] Q. Yuan, Z. Zhou, J. Zhuang, X. Wang, *Chem. Commun.* **2010**, *46*, 1491.

[17] Y. Ito, W. Cong, T. Fujita, Z. Tang, M. Chen, *Angew. Chem. Int. Ed.* **2015**, *54*, 2131.

[18] Y. Zheng, Y. Jiao, Y. Zhu, L. H. Li, Y. Han, Y. Chen, A. Du, M. Jaroniec, S. Z. Qiao, *Nat. Commun.* **2014**, *5*, 3783.

[19] C. Tan, H. Zhang, *J. Am. Chem. Soc.* **2015**, *137*, 12162.

[20] J. D. Benck, Z. Chen, L. Y. Kuritzky, A. J. Forman, T. F. Jaramillo, *ACS Catal.* **2012**, *2*, 1916.

[21] Q. H. Wang, K. Kalantar-Zadeh, A. Kis, J. N. Coleman, M. S. Strano, *Nat. Nanotechnol.* **2012**, *7*, 699.

[22] D. Voiry, M. Salehi, R. Silva, T. Fujita, M. Chen, T. Asefa, V. B. Shenoy, G. Eda, M. Chhowalla, *Nano Lett.* **2013**, *13*, 6222.

[23] M. A. Lukowski, A. S. Daniel, F. Meng, A. Forticaux, L. Li, S. Jin, *J. Am. Chem. Soc.* **2013**, *135*, 10274.

[24] B. Hinnemann, P. G. Moses, J. Bonde, K. P. Jørgensen, J. H. Nielsen, S. Horch, I. Chorkendorff, J. K. Nørskov, *J. Am. Chem. Soc.* **2005**, *127*, 5308.

[25] T. F. Jaramillo, K. P. Jørgensen, J. Bonde, J. H. Nielsen, S. Horch, I. Chorkendorff, *Science* **2007**, *317*, 100.

[26] J. Xie, J. Zhang, S. Li, F. Grote, X. Zhang, H. Zhang, R. Wang, Y. Lei, B. Pan, Y. Xie, *J. Am. Chem. Soc.* **2013**, *135*, 17881.

[27] M.-R. Gao, M. K. Y. Chan, Y. Sun, *Nat. Commun.* **2015**, *6*, 7493.

[28] C. N. R. Rao, A. K. Sood, K. S. Subrahmanyam, A. Govindaraj, *Angew. Chem. Int. Ed.* **2009**, *48*, 7752.

[29] A. K. Geim, K. S. Novoselov, *Nat. Mater.* **2007**, *6*, 183.

[30] Y. Li, H. Wang, L. Xie, Y. Liang, G. Hong, H. Dai, *J. Am. Chem. Soc.* **2011**, *133*, 7296.

[31] X. Zheng, J. Xu, K. Yan, H. Wang, Z. Wang, S. Yang, *Chem. Mater.* **2014**, *26*, 2344.

[32] X. Xie, Z. Ao, D. Su, J. Zhang, G. Wang, *Adv. Funct. Mater.* **2015**, *25*, 1393.

[33] Q. Xiang, J. Yu, M. Jaroniec, *J. Am. Chem. Soc.* **2012**, *134*, 6575.

[34] J. Zhang, L. Dai, *ACS Catal.* **2015**, *5*, 7244.

[35] M. T. Pope, A. Müller, *Angew. Chem. Int. Ed.* **1991**, *30*, 34.

[36] D.-Y. Du, J.-S. Qin, S.-L. Li, Z.-M. Su, Y.-Q. Lan, *Chem. Soc. Rev.* **2014**, *43*, 4615.

[37] D. Zhou, B.-H. Han, *Adv. Funct. Mater.* **2010**, *20*, 2717.

[38] J. Xie, H. Zhang, S. Li, R. Wang, X. Sun, M. Zhou, J. Zhou, X. W. Lou, Y. Xie, *Adv. Mater.* **2013**, *25*, 5807.

[39] S. Chen, J. Duan, Y. Tang, B. Jin, S. Zhang Qiao, *Nano Energy* **2015**, *11*, 11.

[40] Y. Zhao, R. Nakamura, K. Kamiya, S. Nakanishi, K. Hashimoto, *Nat. Commun.* **2013**, *4*, 2390.

[41] Q. Mahmood, S. K. Park, K. D. Kwon, S.-J. Chang, J.-Y. Hong, G. Shen, Y. M. Jung, T. J. Park, S. W. Khang, W. S. Kim, J. Kong, H. S. Park, *Adv. Energy Mater.* **2016**, *6*, 1501115.

[42] S. Zhang, B. V. R. Chowdari, Z. Wen, J. Jin, J. Yang, *ACS Nano* **2015**, *9*, 12464.

[43] N. Zhang, S. Gan, T. Wu, W. Ma, D. Han, L. Niu, *ACS Appl. Mater. Interfaces* **2015**, *7*, 12193.

[44] N. Pentland, J. O. M. Bockris, E. Sheldon, *J. Electrochem. Soc.* **1957**, *104*, 182.

[45] W. Sheng, H. A. Gasteiger, Y. Shao-Horn, *J. Electrochem. Soc.* **2010**, *157*, B1529.

[46] Z. Huang, W. Luo, L. Ma, M. Yu, X. Ren, M. He, S. Polen, K. Click, B. Garrett, J. Lu, K. Amine, C. Hadad, W. Chen, A. Asthagiri, Y. Wu, *Angew. Chem. Int. Ed.* **2015**, *127*, 15396.

[47] Y.-J. Tang, M.-R. Gao, C.-H. Liu, S.-L. Li, H.-L. Jiang, Y.-Q. Lan, M. Han, S.-H. Yu, *Angew. Chem. Int. Ed.* **2015**, *54*, 12928.

[48] J. K. Nørskov, T. Bligaard, A. Logadottir, J. R. Kitchin, J. G. Chen, S. Pandelov, U. Stimming, *J. Electrochem. Soc.* **2005**, *152*, J23.

[49] Y. Liu, G. Yu, G. D. Li, Y. Sun, T. Asefa, W. Chen, X. Zou, *Angew. Chem. Int. Ed.* **2015**, *54*, 10752.